Global J. Environ. Sci. Manage. 7(4): 543-554, Autumn 2021

Global Journal of Environmental Science and Management
(GJESM)

Homepage: https://www.gjesm.net/

ORIGINAL RESEARCH PAPER

Simulation and analysis of marine hydrodynamics based on the El Niño scenario

M. Ikhwan[1], R. Wafdan[2], Y. Haditiar[2], M. Ramli[3], Z.A. Muchlisin[1,4,5], S. Rizal[1,2,5,*]

[1]*Graduate School of Mathematics and Applied Science, Universitas Syiah Kuala, Banda Aceh 23111, Indonesia*

[2]*Department of Marine Sciences, Faculty of Marine and Fisheries, Universitas Syiah Kuala, Banda Aceh 23111, Indonesia*

[3]*Department of Mathematics, Universitas Syiah Kuala, Banda Aceh 23111, Indonesia*

[4]*Department of Aquaculture, Faculty of Marine and Fisheries, Universitas Syiah Kuala, Banda Aceh 23111, Indonesia*

[5]*Research Center for Marine Sciences and Fisheries, Universitas Syiah Kuala, Banda Aceh 23111, Indonesia*

ARTICLE INFO

Article History:
Received 05 January 2021
Revised 19 March 2021
Accepted 23 April 2021

Keywords:
Density
El Niño-Southern Oscillation (El Niño)
Pacific Ocean
Sea level
The fast Fourier transform (FFT)

ABSTRACT

BACKGROUND AND OBJECTIVES: El Niño- Southern Oscillation is known to affect the marine and terrestrial environment in Southeast Asia, Australia, northern South America, and southern Africa. There has been much research showing that the effects of El Niño- Southern Oscillation are extensive. In this study, a simulation of an El Niño event is carried out, which is ideal in the vertical layer of the Pacific Ocean (0-250 meters). The fast Fourier transform is used to process the vertical modeling data so that the results can accurately represent El Niño.

METHODS: A non-hydrostatic 3-dimensional numerical model is used in this research. To separate the signal produced and obtain the quantitative difference of each sea layer, the simulation results are analyzed using the fast Fourier transform. Winds blow from the west to the east of the area in perfect El Niño weather, with a reasonably high wind zone near the equator (forming a cosine). Open fields can be found on the north and south sides, while closed fields can be found on the west and east sides. Density is uniform up to a depth of 100 meters, then uniformly increases by 1 kilogram per cubic meter from 100 to 250 meters.

FINDINGS: The results of the model simulation show that one month later (on the 37th day), the current from the west has approached the domain's east side, forming a complete coastal Kelvin wave. The shape of coastal Kelvin waves in the eastern area follows a trend that is similar to the OSCAR Sea Surface Velocity plot data obtained from ERDDAP in the Pacific Ocean in October 2015. In this period, the density at a depth of 0-100 meters is the same, while the density at the depth layer underneath is different.

CONCLUSION: Strong winds could mix water masses up to a depth of 100 meters, implying that during an ideal El Niño, the stratification of the water column is influenced by strong winds. The eastern domain has the highest sea level amplitude, resulting in perfect mixing up to a depth of 100 m, while wind effect is negligible in the lower layers. The first layer (0-50 m) and the second layer (50-100 m) have the same density and occur along the equator, according to FFT. The density is different and much greater in the third layer (100-150 m).

DOI: 10.22034/gjesm.2021.04.04

NUMBER OF REFERENCES	NUMBER OF FIGURES	NUMBER OF TABLES
31	9	3

*Corresponding Author:
Email: *srizal@unsyiah.ac.id*
Phone: +62 852-5714-9009
Fax: +62 651-7555261

Note: Discussion period for this manuscript open until January 1, 2022 on GJESM website at the "Show Article.

INTRODUCTION

El Niño - Southern Oscillation (ENSO) is a manifestation of the inter-annual variability, but it is associated with major changes in the pacific atmosphere through a phenomenon known as southern oscillation (Chen *et al*., 2019a; Trenberth, 2019). Warming of the tropical Pacific Ocean surface and strengthening equatorial trade winds characterize El Niño events, which occur every few years. During El Niño years, such as 2015/2016, winds from the west are typically symmetrical (Sundararajan, 2020).

The El Niño outbreak in 2015/2016 was caused by a series of westerly wind events in boreal springs. There has been much research showing that the effects of ENSO are extensive. Doughty *et al.* (2021) reported that ENSO affects the tropical forests of the Amazon, which are the world's major CO_2 players, where the rates of photosynthesis, fluorescence, and greenness were above average during El Niño (2009/2010) and below normal during La Nina (2010/2011). Hao *et al.* (2018) shows that ENSO causes dry and hot summer events in such as northern South America, southern Africa, Southeast Asia and Australia. Meanwhile, in East Asia's subtropical forests, El Niño can increase the growth of individual trees through increased sunlight (Li *et al.,* 2020). In the fishing sector, El Niño can cause anomalous fish migration patterns, such as changes in latitudinal migration of sardinella along the African coast (López-Parages *et al.*, 2020). Pécastaing and Chávez (2020) also reported that ENSO makes coastal communities vulnerable to poverty, especially for communities in Peru's arid ecosystems. It must be taken into account that going forward, the potential for El Niño is projected to increase drastically due to the effects of global warming associated with the flattening of thermoclines in the equatorial Pacific (Yeh *et al*., 2009; Chen *et al*., 2019b). El Niño also has relatively strong connections to other oceans. Siswanto *et al.* (2020) imply that low and high trophic level marine organisms in the eastern Indian Ocean were also affected by ENSO. Yue *et al.* (2020) reported that the zone of anomaly induced by wind advection during El Niño affects the Walker circulation and sea surface salinity in the Indian Ocean. In addition, ENSO caused changes in the circulation of the tropical Pacific Walker due to warming in the Indian and Atlantic Oceans (Behera *et al*., 2021). El Niño affects salinity so that one of the parameters to determine the occurrence of El Niño is sea surface salinity (Sharma, 2018). So far, Sundararajan (2020) stated that the wind is an equinoctial symmetry in the 2015 El Niño year. This affects the magnitude of the tidal currents in the Pacific. According to Hu *et al.* (2013), ENSO behavior is influenced by the low-frequency variability of the tropical Pacific climate. These variations include increased warming and local wind variability in the Pacific Ocean's tropical parts (Hu *et al.*, 2013). Since the late 1970s, the ENSO frequency has shifted, with the ENSO frequency being high (2-4 years) in 1962-1975 and low (4-6 years) in 1980-1993 (An and Wang, 2000; Fedorov and Philander, 2000). In 1999-2000, the correlation between warm water volume around the equator and ENSO was also seen to be weaker. According to Horii *et al.* (2012) and McPhaden (2012), this condition relates to the divergence of winds in the central Pacific that inhibits the eastward spread of sea surface temperature anomalies. Weak east-west sea surface temperature gradient provides relaxation to trade winds. Consequently, with weak trade wind conditions, the equatorial upwelling, which carries cooler, high-density water to the pacific surface, is also reduced (Kumar and Hu, 2014). Rizal *et al.* (2019; 2020) found that variations in density gradients influence the form of lee waves and baroclinic currents that contribute to the mainstream in a basin. According to recent studies, the ENSO regime continues to change spatially over time, and this is due to local wind variability. The aim of this study is to determine the properties of the sea level and density as a result of El Niño, which is best modeled using a non-hydrostatic 3D numerical model. The impact of the wind on the sea level and density at each layer is investigated in this paper. In this case, there are two methods for analyzing the data. To begin, graphically, by depicting the density in each layer. Second, by comparing the magnitudes of each layer density and sea level of first layer using the fast Fourier transform (FFT) process. To date, to the authors' knowledge, there is no research that has examined this issue in detail using the FFT. This study also contributes to the Pacific's subsurface investigation. This study has been carried out in the Ocean Modelling Laboratory, Department of Marine Sciences, Universitas Syiah Kuala, Indonesia in 2020.

MATERIALS AND METHODS

Winds from the west are generally symmetrical during El Nino years as was the case in 2015/2016.

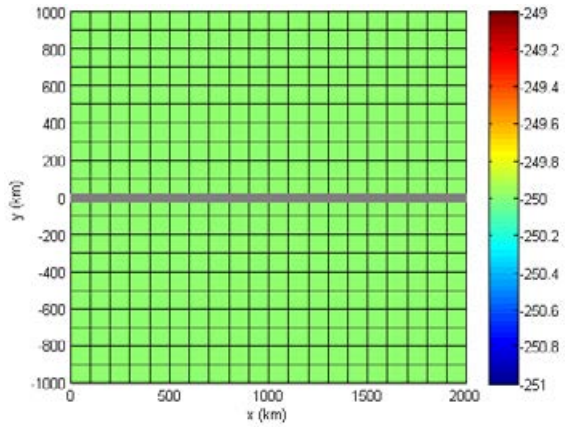

(a)

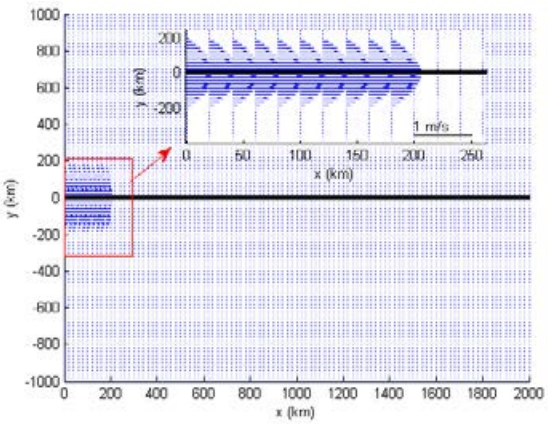

(b)

Fig. 1: Model setup (a) domain model, (b) wind stress force

A sequence of westerly wind events in boreal spring triggered the most recent El Niño outbreak in 2015/2016. Downwelling oceanic Kelvin waves were caused by the associated wind forcing, minimizing the upwelling of cold subsurface waters in the eastern Pacific cold tongue and resulting in surface warming in the central and eastern Pacific (Timmermann *et al.*, 2018). The emergence of Downwelling is a product of the effect of winds on the Pacific's surface. As a result, it is important that we obtain a model of the Pacific's surface layer. It's also crucial to understand how much wind is always blowing. Meanwhile, the most recent El Niño outbreak, which occurred in 2015/2016, was triggered by a series of westerly wind events in boreal spring. In the pacific model, this condition is applied as a force. The three-dimensional numerical model is efficient enough to represent low-resolution circulating currents. The current model is based on hydrostatic primitive equations, such as those proposed by Cha *et al.* (2018) and Peng *et al.* (2020). Cha *et al.* (2018) used a three-dimensional model to observe a distinct low-frequency mode of the tropical Pacific sea level and display its connection to global ocean warming. Meanwhile, this research employs a non-hydrostatic technique that has previously been used to model tides in the Malacca Strait (Haditiar *et al.*, 2020), internal wave (Rizal *et al.*, 2019), and Lee waves (Rizal *et al.*, 2020). A non-hydrostatic method may be used to explain the mechanism of the Lee wave, as well as the internal wave. Numerical experiments were carried out based on Kämpf (2010). This study has a domain model with a horizontal boundary of 2,000 × 2,000 km and a uniform depth of 250 m (see Fig. 1(a)).

The lateral grid distance is $\Delta x = \Delta y = 20$ km, while the vertical grid distance is $\Delta z = 50$ m so that it forms five layers with time step $\Delta t = 120$ seconds. In the west and east, closed boundaries are defined, likened to a dry area (coast). Furthermore, the north and south sides of the model domain are given open boundaries. The sea's initial condition is at rest, and this model uses a free-surface so that the numerical time steps will last a long time. The seawater density at 100 m and above from the bottom is 1027 kg/m^3, while below it is 1028 kg/m^3. The internal gravity wave phase velocity associated with this density configuration is $c = 0.75$ m/s. This value is obtained using the equatorial beta-plane approximation using Eq. 1.

$$f = \beta y \tag{1}$$

where, y is the meridional coordinate, and β is the set of $\beta = 2.5 \times 10^{-11}$ 1/ms. This model is given a wind force from the Westside, which consists of wind stress moving eastward in the form of cosine in the y-direction (Fig. 1(b)). The maximum magnitude is 0.1 Pa at the equator, and the wind stress force is applied within 200 km from the west side. Wind stress magnitude will be stopped after the first five days of simulation.

Cyclic boundary conditions are used in open boundaries on the North (ny and ny+1) and South sides (0 and 1). This cyclic boundary condition uses

Table 1: The procedure for achieving outcomes

Process	In-process information
1	To get the sea level and density performance, run the Kämpf model simulation in Fortran.
2	Display and retrieve/sample the desired performance data for sea level and density.
3	The output is displayed after searching for the FFT value.

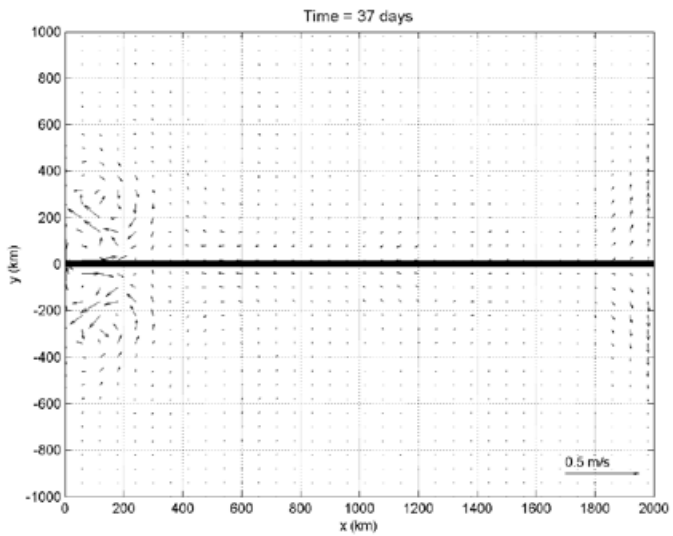

Fig. 2: Currents plot on the 37th day of simulation

the "mirror" condition for the meridional flow component (*i*-index) in Eq. 2 and 3 (Haditiar *et al.*, 2019).

$$v(i,0,k) = -v(i,ny,k) \tag{2}$$

$$v(i,ny+1,k) = -v(i,1,k) \tag{3}$$

The advanced turbulence closure scheme introduced by Smagorinsky (1963) was applied to parameterize lateral eddy viscosity and diffusivity (A_h). Here is the equation using Eq. 4.

$$A_h = c_1 \Delta x \Delta y \sqrt{\left(\frac{\partial u}{\partial x}\right)^2 + \left(\frac{\partial v}{\partial y}\right)^2 + 0{,}5\left(\frac{\partial u}{\partial y} + \frac{\partial v}{\partial x}\right)^2} \tag{4}$$

Where, c_1 is a parameter with a value between 0.1 and 0.2. The value of c_1 chosen in this study was 0.1. The simulation was run several times with the procedure listed in Table 1.

RESULTS AND DISCUSSION

This El Niño model simulation is run for 60 days with time step Δt = 120 seconds. This simulation generates current, sea level, and density data, which will be analyzed to determine sea level and density. Furthermore, the data is stored every 12 hours of simulation. In this article, the simulation output data for day 37 is analyzed because the coastal Kelvin waves have formed correctly on the East side (Fig. 2). The formation of coastal Kelvin waves in the eastern region follows a similar pattern as the OSCAR Sea Surface Velocity plot data obtained from ERDDAP in October 2015 in the Pacific Ocean (Fig. 3). Fig. 2 simulation and Fig. 3 observation are not identical. Since, Fig. 2 is based on ideal bathymetry, wind, and shoreline, whereas Fig. 3 is based on real bathymetry, wind, and shoreline.

The plot of sea level simulation results on the 37th day can be seen in Fig. 4. From the sea-level value in Fig. 4(a), the sea level value is taken at x = 400 km, called the western part, x = 1200 km is called

the middle part, and x = 1980 km is called the eastern part. In the three sections, the results are obtained, as shown in Fig. 4(b). Sea level in the western part is negative around the equator and is positive in areas far from the equator. Furthermore, in the middle part, the sea level value shows the same properties as the sea level value in the western part. However, in the western part, sea level has a steeper graph at the equator than in the middle. In contrast to the two sea-level values, the data in the eastern part can be observed that all values are positive, but at the equator, it forms a peak with a value of 1.58 cm while on the North and South sides, which are far from the equator a value of 0.24 cm. The variation in sea level away from the equator is influenced by local and remote responses (Chang *et al*., 2013).

Fig. 5 shows the density value of seawater at the equator. It can be observed that the densities at 0-50 m and 50-100 m depths show a similar pattern of change on the 37th day. The density at these two depths shows the same properties after being given a wind force until the end of the

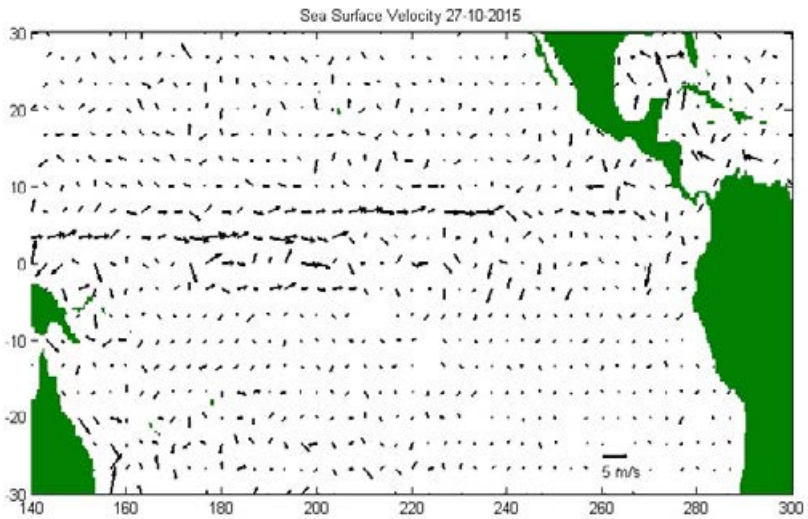

Fig. 3: Sea surface velocity on October 2015

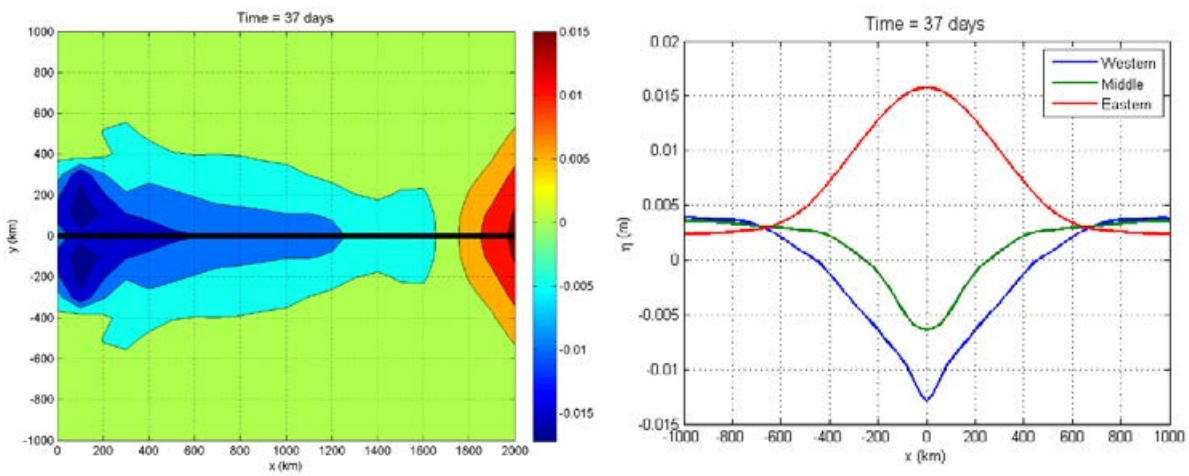

(a) (b)

Fig. 4: Sea level (a) plot on the 37th day of simulation, (b) value at the equator on the 37th day

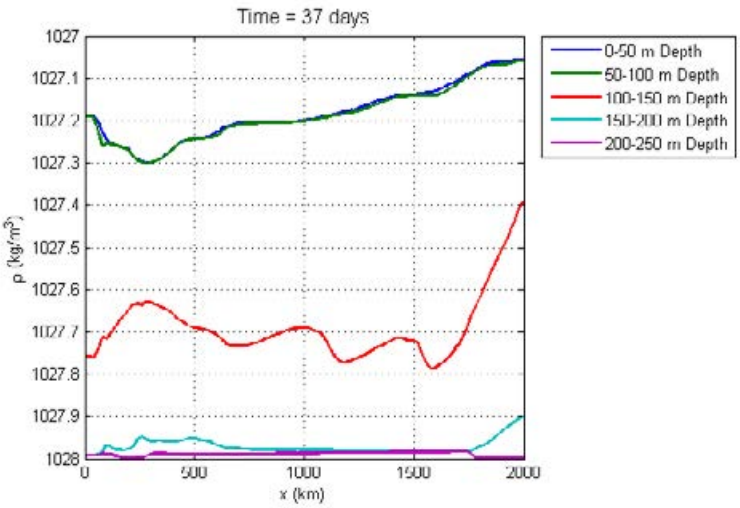

Fig. 5: The value of density at the equator at 37 days of simulation

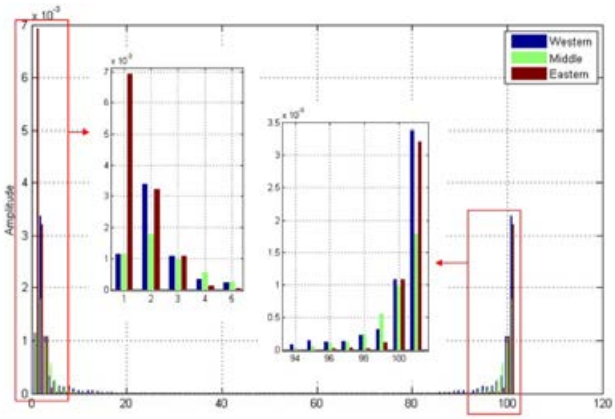

(a)

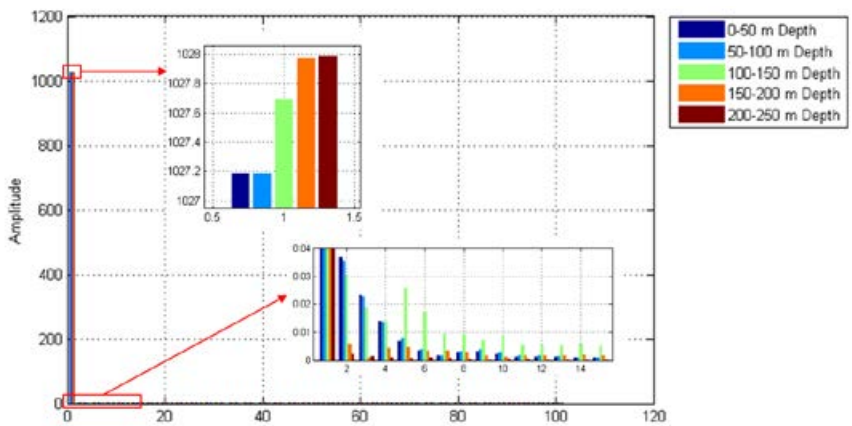

(b)

Fig. 6: The FFT value at the equator on the 37th day of (a) the sea level, (b) the density

Table 2: Amplitude, frequency, and phase of sea level values

i	Western		
	A_s	*F*	θ
1	0.00338	0.10000	0.03100
2	0.00338	10.00000	-0.03100
3	0.00115	0.00000	3.14159
4	0.00108	0.20000	-3.07910
5	0.00108	9.90000	3.07910
6	0.00032	0.30000	0.09086
7	0.00032	9.80000	-0.09086
i	Middle		
	A_s	*F*	θ
1	0.00179	0.10000	0.03096
2	0.00179	10.00000	-0.03096
3	0.00115	0.00000	0.00000
4	0.00096	0.20000	-3.07977
5	0.00096	9.90000	3.07977
6	4.00000	0.00055	0.30000
7	99.00000	0.00055	9.80000
i	Eastern		
	A_s	*F*	θ
1	0.00693	0.00000	0.00000
2	0.00321	0.10000	-3.11051
3	0.00321	10.00000	3.11051
4	0.00108	0.20000	0.06226
5	0.00108	9.90000	-0.06226
6	0.09305	0.00011	0.30000
7	-0.09305	0.00011	9.80000

simulation, in contrast to the density at a depth of 100-250 m. Densities at a depth of 100-150 m have begun to show changes in density values ranging between 1027.4 kg/m^3 and 1027.8 kg/m^3. At a depth of 150-200 m and 200-250 m, the density, in general, does not change significantly but shows a different pattern. This simulation generates current, sea level, and density data, which will be analyzed to determine sea level and density. The formation of Ekman and Kelvin waves is used to compare experiments theoretically. During the El Nino phase, Kelvin waves are thought to migrate into the eastern Pacific Ocean (Kämpf, 2010; Capotondi *et al.,* 2019). Meanwhile, the Ekman layer (D_E) can be approximated using Eq. 5 (Kämpf, 2010).

$$D_E = \sqrt{\frac{2\pi^2 A_z}{f}} = \frac{7.6}{\sqrt{\sin|\varphi|}} U_{10} \quad (5)$$

The Ekman layer is related to a three-dimensional wind-driven circulation model, such as the one used in experiment. The Ekman layer is a thin layer that allows the wind's effects to continue to function. If the highest wind stress is wind = 0.1 pa and the wind speed is U_{10} = 5.5 m/s, the Ekman layer (D_E) at the equator is the deepest, while it can reach 220 meters at 200 km from the equator using Eq. 6.

$$(U_{10} = \sqrt{\frac{\tau^{wind}}{\rho_{air} C_d}}, \text{ where } \rho_{air} = 1.25 \text{ dan } C_d = 2.6 \text{x} 10^{-3}) \quad (6)$$

Meanwhile, the most recent El Niño outbreak,

Table 3: Amplitude, frequency, and phase of the density values

i	0-50 m Depth		
	A_d	F	θ
1	1027.18267	0.00000	0.00000
2	0.03675	0.10000	-1.78340
3	0.03675	10.00000	1.78340
4	0.02330	0.20000	-1.82001
5	0.02330	9.90000	1.82001
6	0.01407	0.30000	-2.18821
7	0.01407	9.80000	2.18821
i	50-100 m Depth		
	A_d	F	θ
1	1027.18668	0.00000	0.00000
2	0.03566	0.10000	-1.76912
3	0.03566	10.00000	1.76912
4	0.02291	0.20000	-1.82199
5	0.02291	9.90000	1.82199
6	0.01371	0.30000	-2.14562
7	0.01371	9.80000	2.14562
i	100-150 m Depth		
	A_d	F	θ
1	1027.68937	0.00000	0.00000
2	0.03006	0.10000	2.86144
3	0.03006	10.00000	-2.86144
4	0.02565	0.40000	-1.70419
5	0.02565	9.70000	1.70419
6	0.01878	0.20000	-2.77093
7	0.01878	9.90000	2.77093
i	150-200 m Depth		
	A_d	F	θ
1	1027.97072	0.00000	0.00000
2	0.00600	0.10000	2.55146
3	0.00600	10.00000	-2.55146
4	0.00473	0.40000	-1.98551
5	0.00473	9.70000	1.98551
6	0.00452	0.30000	-1.79668
7	0.00452	9.80000	1.79668
i	200-250 m Depth		
	A_d	F	θ
1	1027.98959	0.00000	0.00000
2	0.00216	0.10000	-0.52145
3	0.00216	10.00000	0.52145
4	0.00136	0.20000	0.34275
5	0.00136	9.90000	-0.34275
6	0.00103	0.50000	2.48266
7	0.00103	9.60000	-2.48266

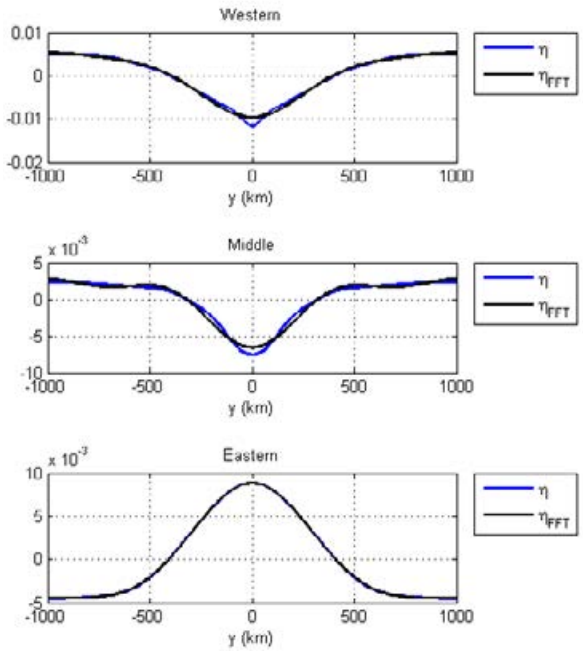

Fig. 7: Sea level plot from the FFT results

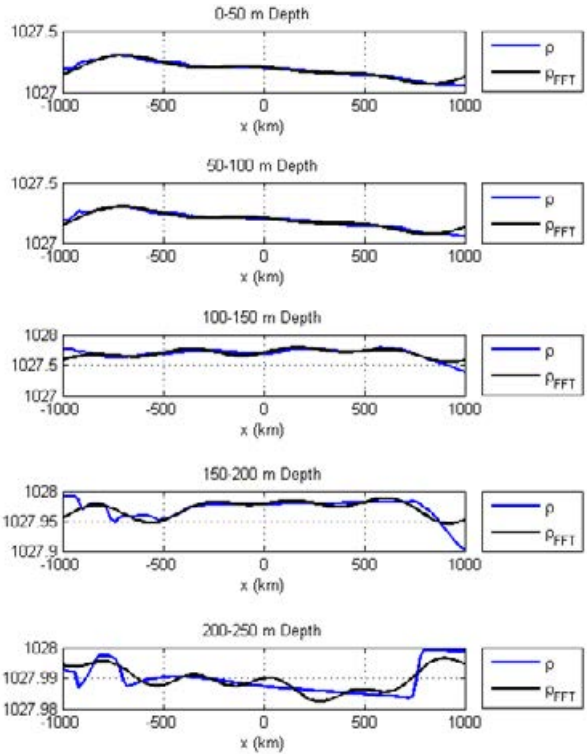

Fig. 8: The density plot of each layer depth from the FFT results

which occurred in 2015/2016, was triggered by a series of westerly wind events in boreal spring. In the pacific model, this condition is applied as a force. In this experiment, we attempted to evaluate the El Niño phenomenon described by ideal winds by examining the numerical effects of the pacific model (which included tides, sea level, and density changes). An analytical approach, namely FFT, was used to carry out further research. The variations and amplitudes of each fluid layer can be calculated analytically using FFT.

The next step is to find FFT value from the sea-level value. Fig. 6(a) shows the magnitude of sea-level plots in the western, central, and eastern parts on the 37th day. From this graph, seven data were selected with the enormous output magnitude from FFT for sea-level values consisting of amplitude, frequency, and phase values (see Table 2). The enormous amplitude value of sea level in the western part is 0.00338 m. Furthermore, the enormous amplitude value from sea level in the middle is 0.00179 m and in the eastern part is 0.00693 m. Of the three regions, the eastern part of the domain has the largest amplitude, namely 0.00693 m. Table 2 shows two amplitude and frequency values of sea level values in the West and the center that have the same value, but the phase values are different. Furthermore, using Eq. 7 with n = 7 where i is the data index and the amplitude, frequency, and phase values in Table 2 and Fig. 7 can be obtained. This figure shows that with the seven data available in Table 2, most of them can represent the sea level data generated from the simulation using Eq. 7.

$$f(t)=\sum_{i=1}^{n}A_i\cos\left(2\pi F_i t+\theta_i\right) \quad (7)$$

Next, for density data, the amplitude, frequency, and phase values are also searched using the FFT. Fig. 6(b) shows a magnitude plot of the densities at depths of 0-50 m, 50-100 m, 100-150 m, 150-200 m, and 200-250 m at the equator on the 37th day. Seven data sets with an enormous magnitude are selected from the FFT output for density values (Table 3). An enormous amplitude value of the density at a depth of 0-50 m is 1027.18267 kg/m^3. An enormous amplitude value of the density at a depth of 50-100 m is 1027.18668 kg/m^3. An enormous amplitude value of the density at a depth of 100-150 m is 1027.68937

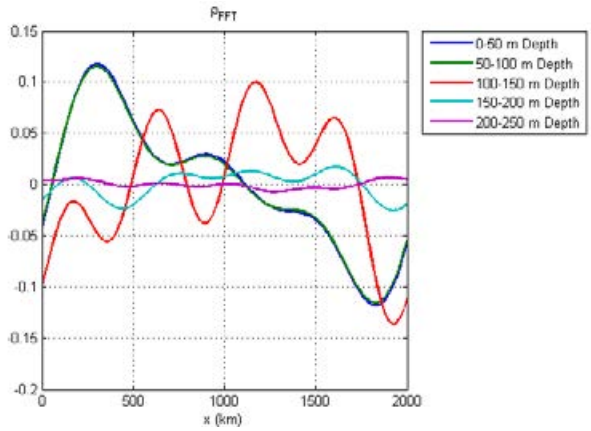

Fig. 9: The density value of the FFT results at y = 0

kg/m^3. An enormous amplitude value of the density at a depth of 150-200 m is 1027.97072 kg/m^3. An enormous amplitude value of the density at a depth of 200-250 m is 1027.98959 kg/m^3. Of the five layers of depth, the depth of 150-200 m has the largest amplitude with a value of 1027.98959 kg/m^3.

Table 3 can also be observed that the amplitude, frequency, and phase at a depth of 0-50 m and 50-100 m have almost the same values. Then, using Eq. 7 with n = 7 and the amplitude, frequency, and phase values in Table 3, the graph is obtained in Fig. 8. This figure shows that with the seven data available in Table 3, most of them can already represent the density data generated from the simulation.

If the graph of each layer is shifted to y = 0, the result is shown in Fig. 9. From the figure, it can be seen that the density values of the FFT results for a depth of 0-50 m and 50-100 m are almost coincided, which means that the density at a depth of 0-50 m and 50-100 m has the same change pattern after being given a wind force on the sea surface.

CONCLUSION

In the 37 days of simulations of an ideal El Niño event in the Pacific Ocean, the current has entered the East and created a complete coastal Kelvin wave. In the eastern region, the shape of coastal Kelvin waves follows a pattern similar to the OSCAR Sea Surface Velocity plot data obtained from ERDDAP in the Pacific Ocean in October 2015. Around the equator, the sea-level value is negative in the western and middle regions, but positive in areas far from the equator. The western part's sea-level value, on the other hand, has a steeper graph at the equator than the middle. The FFT findings also reveal that there are two amplitude and frequency values for the sea level values in the West and East that are the same, but the phase values are different. The eastern part of the domain has the highest amplitude of the three parts, according to FFT data. In addition, there are two amplitude and frequency values from sea level values in the West and East that are the same, but the phase values are different. Both graphically and from the FFT, densities at depths of 0-50 m and 50-100 m display a similar pattern of changes on the 37th day. Despite having given the wind force until the end of the simulation, the density at these two depth layers has the same properties as the density at the depth below, which is different from the density at the depth below. It's caused by wind forces operating at a depth of 0-100 meters. Meanwhile, wind impact is very weak or non-existent at depths of 100-150 m, 150-200 m, and 200-250 m. The density does not change significantly between 150-200 m and 200-250 m, but it does follow a different pattern. The vertical density stratification decreases from five to four layers in general. At depths of 0-50 m and 50-100 m, the amplitude, frequency, and phase are nearly identical.

AUTHOR CONTRIBUTIONS

M. Ikhwan performed the literature review, running the model, analyzed and interpreted the data, prepared the manuscript text, and manuscript edition. R. Wafdan performed the literature review, running the model, analyzed and interpreted the data, prepared the manuscript text, and manuscript edition. Y. Haditiar performed the literature review, prepared numerical code, prepared the manuscript text, and manuscript edition. M. Ramli performed the literature review, analyzed and interpreted the data, prepared the manuscript text, and manuscript edition. Z.A. Muchlisin performed the literature review, prepared the manuscript text, and manuscript edition. S. Rizal performed the literature review, experimental design, analyzed and interpreted the data, prepared the manuscript text, and manuscript edition.

ACKNOWLEDGEMENT

This study is funded by Universitas Syiah Kuala, Banda Aceh, Ministry of Education and Culture, Indonesia, under the scheme of the Professor

research [contract number: 11/UN11.2.1/PT.01.03/PNBP/2020] and *'Program Riset Unggulan Universitas Syiah Kuala Percepatan Doktor'* [contract number: 300/UN11.2/PP/PNBP/SP3/2019].

CONFLICT OF INTEREST

The authors declare no potential conflict of interest regarding the publication of this work. In addition, the ethical issues including plagiarism, informed consent, misconduct, data fabrication and, or falsification, double publication and, or submission, and redundancy have been completely witnessed by the authors.

ABBREVIATIONS

Δt	Time-step, s
Δx, Δy , Δz	Distance spacing, m
β	Meridional variation of Coriolis parameter, $\beta = 2.5 \times 10^{-11}$ 1/ms
ρ	Seawater density, kg/m^3
θ	Phase of density, degree
τ	Wind stress, pa
A_d	Amplitude of density, kg/m^3
A_h	Horizontal eddy viscosity, m^2/s
A_s	Amplitude of sea level, m
c	Phase speed of internal gravity waves, m/s
c_1	Free parameter for turbulence closure scheme, non-dimensional
D_E	The Ekman layer
ENSO	El Niño – Southern Oscillation
Eq.	Equation
f	Coriolis parameter, 1/s
F	Frequency of density, Hz
Fig.	Figure
FFT	Fast Fourier Transform
Hz	Hertz
kg/m^3	kilogram per meter cubic
km	kilometers
m	meters
1/ms	one per meter second
m/s	meter per second
Pa	Pascal
U_{10}	Wind speed at 10 m above sea level, m/s
u,v	Currents, m/s
y	Meridional coordinate, m

REFERENCES

An, S.I.; Wang, B., (2000). Interdecadal change of the structure of the ENSO mode and its impact on the ENSO frequency. J. Clim., 13(12): 2044-2055 **(12 pages)**.

Behera, S.K.; Doi, T.; Luo, J.J., (2021). Air–sea interaction in tropical Pacific: The dynamics of El Niño/Southern Oscillation. Tropical and Extratropical Air-Sea Interactions. Elsevier.

Capotondi, A.; Sardeshmukh, P.D.; Lorenzo, E.D.; Subramanian, A.C; Miller, A.F., (2019). Predictability of US West Coast Ocean Temperatures is not solely due to ENSO. Sci. Rep., 9: 10993 **(10 pages)**.

Cha, S.; Moon, J.; Song, Y.T., (2018). A recent shift toward an El Niño-like ocean state in the tropical Pacific and the resumption of ocean warming. Geophysical Research Letters, 45: 11,885–11,894 **(10 pages)**.

Chang, Y.T.; Du, L.; Zhang, S.W.; Huang, P.F., (2013). Sea level variations in the tropical Pacific Ocean during two types of recent El Niño events. Global Planet. Change, 108: 119–127 **(9 pages)**.

Chen, N.; Thual, S.; Stuecker, M.F., (2019a). El Niño and the Southern Oscillation: Theory. Reference Module in Earth Systems and Environmental Sciences. Elsevier.

Chen, N.; Thual, S.; Hu, S., (2019b). El Niño and the Southern Oscillation: Observation. Reference Module in Earth Systems and Environmental Sciences. Elsevier.

Doughty, R.; Xiao, X.; Qin, Y.; Wu, X.; Zhang, Y.; Moore, B., (2021). Small anomalies in dry-season greenness and chlorophyll fluorescence for Amazon moist tropical forests during El Niño and La Niña. Remote Sens. Environ., 253: 112196 **(8 pages)**.

Fedorov, A.V.; Philander, S.G., (2000). Is El Niño changing? Science, 288(5473): 1997-2002 **(6 pages)**.

Haditiar, Y; Putri, M.R.; Ismail, N.; Muchlisin, Z.A.; Rizal, S., (2019). Numerical Simulation of Currents and Volume Transport in the Malacca Strait and Part of South China Sea. Eng. J., 23(6): 129–143 **(5 pages)**.

Haditiar, Y; Putri, M.R.; Ismail, N.; Muchlisin, Z.A.; Ikhwan, M.; Rizal, S., (2020). Numerical study of tides in the Malacca Strait with a 3-D model. Heliyon, 6: e04828 **(16 pages)**.

Hao, Z.; Hao, F.; Singh, V.P.; Zhang, X., (2018). Quantifying the relationship between compound dry and hot events and El Niño–southern Oscillation (ENSO) at the global scale. J. Hydrol., 567: 332–338 **(7 pages).**

Horii, T.; Ueki, I.; Hanawa, K., (2012). Breakdown of ENSO predictors in the 2000s: Decadal changes of recharge/discharge-SST phase relation and atmospheric intraseasonal forcing. Geophys. Res. Lett., 39(10): L10707 **(5 pages)**.

Hu, Z.Z.; Kumar, A.; Ren, H.L.; Wang, H.; L'Heureux, M.; Jin, F.F., (2013). Weakened interannual variability in the tropical Pacific Ocean since 2000. J. Clim., 26(8): 2601-2613 **(13 pages)**.

Kämpf, J., (2010). Advanced ocean modelling: using open-source software. Springer Science & Business Media., New York.

Kumar, A.; Hu, Z.Z., (2014). Interannual and interdecadal variability of ocean temperature along the equatorial Pacific in conjunction with ENSO. Clim. Dyn., 42(5-6): 1243-1258 **(16 pages)**.

Li, J.; Huang, J.G.; Tardif, J.C.; Liang, H.; Jiang, S.; Zhu, H.; Zhou, P., (2020). Spatially heterogeneous responses of tree radial growth to recent El Niño southern-oscillation variability across East Asia subtropical forests. Agric. For. Meteorol., 287: 107939 **(12 pages)**.

López-Parages, J.; Auger, P.A.; Rodríguez-Fonseca, B.; Keenlyside, N.; Gaetan, C.; Rubino, A.; Arisido, M.W.; Brochier, T., (2020). El Niño as a predictor of round sardinella distribution along the northwest African coast. Prog. Oceanogr., 186: 102341 **(40 pages)**.

McPhaden, M.J., (2012). A 21st century shift in the relationship between ENSO SST and warm water volume anomalies. Geophys. Res. Lett., 39(9): L09706 **(5 pages)**.

Pécastaing, N.; Chávez, C., (2020). The impact of El Niño phenomenon on dry forest-dependent communities' welfare in the northern coast of Peru. Ecol. Econ., 178: 106820 **(10 pages)**.

Peng, Q.; Xie, S.; Wang, D.; Kamae, Y.; Zhang, H.; Hu, S.; Zheng, X.; Wang, W., (2020). Eastern Pacific Wind Effect on the Evolution of El Niño: Implications for ENSO Diversity. Journal of Climate, 33(8): 3197-3212 **(6 pages)**.

Rizal, S.; Iskandar, T.; Muhammad; Haditiar, Y.; Ilhamsyah, Y.; Setiawan, I.; Sofyan, H., (2019). Numerical study of the internal wave behaviour in the vertical ocean slice model. J. Eng. Sci. Technol., 14(5): 2836-2846 **(11 pages)**.

Rizal, S.; Wafdan, R.; Haditiar, Y.; Ramli, M.; Halfiani, V., (2020). Numerical study of lee waves characteristics in the ocean. J. Eng. Sci. Technol., 15(2): 1056-1078 **(23 pages)**.

Sharma, N., (2018). Salinity from SMAP radiometer can monitor El Nino. J. Mar. Syst., 187: 141–145 **(5 pages)**.

Siswanto, E.; Horii, T.; Iskandar, I.; Gaol, J.L.; Setiawan, R.Y.; Susanto, R.D., (2020). Impacts of climate changes on the phytoplankton biomass of the Indonesian Maritime Continent. J. Mar. Syst., 212: 103451 **(15 pages)**.

Smagorinsky, J., (1963). General circulation experiments with the primitive equations: I. The basic experiment. Mon. Weather Rev., 91(3): 99-164 **(66 pages)**.

Sundararajan, S., (2020). Equatorial upper mesospheric mean winds and tidal response to strong El Niño and La Niña. J. Atmos. Solar-Terrestrial Phys., 202: 105270 **(7 pages)**.

Timmermann, A.; An, S.; Kug, J.; Jin, F.; Cai, W.; Capotondi, A.; Cobb, K.M.; Lengaigne, M.; McPhaden, M.J; Stuecker, M.F.; Stein, K.; Wittenberg, A.T.; Yun, K.; Bayr, T.; Chen, H.; Chikamoto, Y.; Dewitte, B.; Dommenget, D.; Grothe, P.; Guilyardi, E.; Ham, Y; Hayashi, M.; Ineson, S.; Kang, D.; Kim, S.; Kim, W.; Lee, J.; Li, T.; Luo, J.; McGregor, S.; Planton, Y.; Power, S.; Rashid, H.; Ren, H; Santoso, A.; Takahashi, K.; Todd, A.; Wang, G.; Wang, G.; Xie, R.; Yang, W.; Yeh, S.; Yoon, J.; Zeller, E.; Zhang, X., (2018). El Niño□Southern Oscillation complexity. Nature, **559:** 535–545 **(11 pages)**.

Trenberth, K.E., (2019). El Niño Southern Oscillation (ENSO). Encyclopedia of Ocean Sciences., 6: 420-432 **(13 pages)**.

Yeh, S.W.; Kug, J.S.; Dewitte, B.; Kwon, M.H.; Kirtman, B.P.; Jin, F.F., (2009). El Niño in a changing climate. Nature, 461(7263): 511-514 **(4 pages)**.

Yue, W.; Lin, L.; Xiaotong, Z., (2020). Influence of El Niño events on sea surface salinity over the central equatorial Indian Ocean. Environ. Res., 182: 109097 **(7 pages)**.

AUTHOR (S) BIOSKETCHES

Ikhwan, M., Ph.D. Candidate, Graduate School of Mathematics and Applied Science, Universitas Syiah Kuala, Banda Aceh 23111, Indonesia. Email: *m.ikhwan@mhs.unsyiah.ac.id*

Wafdan, R., M.Sc., Instructor, Department of Marine Sciences, Faculty of Marine and Fisheries, Universitas Syiah Kuala, Banda Aceh 23111, Indonesia. Email: *redjawavdhan11@gmail.com*

Haditiar, Y., Ph.D., Assistant Professor, Department of Marine Sciences, Faculty of Marine and Fisheries, Universitas Syiah Kuala, Banda Aceh 23111, Indonesia. Email: *yudi.haditiar@gmail.com*

Ramli, M., Ph.D., Professor, Department of Mathematics, Universitas Syiah Kuala, Banda Aceh 23111, Indonesia.
Email: *marwan.math@unsyiah.ac.id*

Muchlisin, Z.A., Ph.D., Professor, [1]Graduate School of Mathematics and Applied Science, Universitas Syiah Kuala, Banda Aceh 23111, Indonesia. [2]Department of Aquaculture, Faculty of Marine and Fisheries, Universitas Syiah Kuala, Banda Aceh 23111, Indonesia. [3]Research Center for Marine Sciences and Fisheries, Universitas Syiah Kuala, Banda Aceh 23111, Indonesia.
Email: *muchlisinza@unsyiah.ac.id*

Rizal, S., Ph.D., Professor, [1]Graduate School of Mathematics and Applied Science, Universitas Syiah Kuala, Banda Aceh 23111, Indonesia. [2]Department of Marine Sciences, Faculty of Marine and Fisheries, Universitas Syiah Kuala, Banda Aceh 23111, Indonesia. [3]Research Center for Marine Sciences and Fisheries, Universitas Syiah Kuala, Banda Aceh 23111, Indonesia. Email: *srizal@unsyiah.ac.id*

HOW TO CITE THIS ARTICLE

Ikhwan, M.; Wafdan, R.; Haditiar, Y.; Ramli, M.; Muchlisin, Z.A.; Rizal, S., (2021). Simulation and analysis of marine hydrodynamics based on the El Niño scenario. Global J. Environ. Sci. Manage., 7(4): 543-554.

DOI: 10.22034/gjesm.2021.04.04

url: https://www.gjesm.net/article_243711.html